ACS APPLIED MATERIALS & INTERFACES

Research Article

www.acsami.org

Highly Responsive Room-Temperature Hydrogen Sensing of α-MoO_3 Nanoribbon Membranes

Shulin Yang,[†] Zhao Wang,[†] Yongming Hu,*[,†] Xiantao Luo,[†] Jinmei Lei,[†] Di Zhou,[§] Linfeng Fei,[‡] Yu Wang,[‡] and Haoshuang Gu*[,†]

[†]Hubei Collaborative Innovation Centre for Advanced Organic Chemical Materials, Faculty of Physics and Electronic Science, Hubei University, Wuhan, Hubei Province, People's Republic of China

[‡]Department of Applied Physics and Materials Research Centre, The Hong Kong Polytechnic University, Hong Kong SAR, People's Republic of China

[§]School of Physics and Information Engineering, Jianghan University, Wuhan, Hubei Province, People's Republic of China

ABSTRACT: [001]-Oriented α-MoO_3 nanoribbons were synthesized via hydrothermal method at temperature from 120 to 200 °C and following assembled a membrane on interdigital electrodes to form sensors. The sensitivity, response speed, and recovery speed of the sensor improve with the increasing hydrothermal temperature. Among them, the sample obtained at 200 °C exhibits a room-temperature response time of 14.1 s toward 1000 ppm of H_2. The nanoribbons also show good selectivity against CO, ethanol, and acetone, as well as high sensitivity to H_2 with a concentration as low as 500 ppb. The hydrogen sensing behavior is dependent on the redox reaction between the H_2 and chemisorbed oxygen species. Higher hydrothermal temperature creates larger specific surface area and higher Mo^{5+} content, leading to increased chemisorbed oxygen species on the nanoribbon surface.

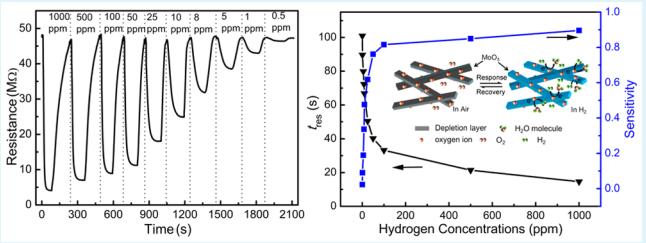

KEYWORDS: *MoO_3, nanoribbons, hydrothermal method, interdigital electrode, hydrogen sensor*

1. INTRODUCTION

For decades, researchers have been developing new ways to harness alternative energy sources in wake of the eventual depletion of fossil fuel.[1] Hydrogen (H_2) is one of the most promising clean energy carriers and has been considered as an alternative to traditional fossil energy sources.[2] However, its small molecule makes H_2 prone to leakage during production, storage, and transportation, which pose serious fire and combustion hazards. As a result, hydrogen sensors are required for monitoring hydrogen concentration and detecting its leakage and diffusion. In the past 20 years, hydrogen sensors based on metal oxide semiconductors have attracted tremendous attention due to their unique advantages such as high sensitivity, long working life, low cost, and good compatibility to silicon microfabrication.[3,4] However, most semiconductor hydrogen sensors have to operate at high temperature (200−400 °C), which consumes a large amount of electricity and poses potential safety hazards during the testing process. Moreover, the sensors also suffer from poor selectivity because at such a high working temperature they will respond to a number of reducing gases with relatively high sensitivities.

One-dimensional (1D) semiconductor metal oxide (SMO) materials have been widely used as gas sensing materials due to their large specific surface area.[5,6] The large number of surface defects provides absorption sites for the gas molecule and atom, hence achieving improved gas sensing performance at low temperature. For example, individual semiconductor oxide nanowire made from ZnO or SnO_2 exhibits remarkable room-temperature (RT) sensing performance to low H_2 concentration, good repeatability, and short response/recovery time.[7] But sensors based on individual SMO nanowire suffer from poor mechanical stability, a complex and expensive fabrication process (e.g., electron beam lithography, etc.), and a narrow detection range. On the other side, multiple nanowires can be assembled into arrays and networks to remediate the mechanical stability and detection range. However, the RT response time of these array sensors is too long to be useful in practical applications. For instance, the response time of hydrogen sensor based on ZnO nanorods is 60 s for 1000 ppm of H_2 at RT,[8] and that of Pd-decorated Nb_2O_5 nanowires is 473 s.[9] Wang et al. have reported an on-chip hydrogen sensor based on self-assembled SnO_2 nanowire on comb-shaped interdigital electrodes (IDEs), which only shows fast response to hydrogen gas at 200−300 °C.[10] Although Pd decoration can improve the RT hydrogen sensing performance of SnO_2 nanowires, it adversely affects the long-term stability owing to Pd pulverization induced by hydrogen adsorption and desorption.[11] Moreover, little is known about the relations between synthetic process and response properties, a key step for

Received: March 2, 2015
Accepted: April 14, 2015
Published: April 14, 2015

DOI: 10.1021/acsami.5b01858
ACS Appl. Mater. Interfaces 2015, 7, 9247−9253

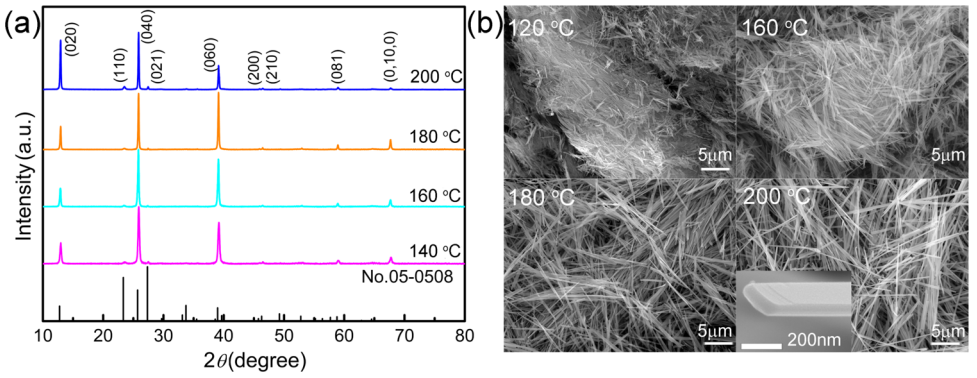

Figure 1. (a) XRD patterns and (b) SEM images of as-prepared samples synthesized at different reaction temperatures.

understanding sensing mechanisms and performance optimization.

Nanostructured molybdenum trioxide (MoO_3) possesses interesting physical and chemical characteristics such as high electrochemical activity, low thermal dynamic stability and high specific surface area. Pure MoO_3 can exist in three different polymorphs, namely the thermodynamically stable orthorhombic phase (α-MoO_3), the metastable monoclinic phase (β-MoO_3) and the hexagonal phase (h-MoO_3). Among them, α-MoO_3 with layered structure has been widely used in biochemistry,[12] lithium ion battery,[13] photocatalysis,[14] and gas sensors.[5] Each layer of α-MoO_3 is consisting of double-layered MoO_6 octahedra with shared corners, and combined with each other by weak van der Waals forces along the b axis. This layered structure has relatively higher tolerance to non-stoichiometry such as the unusual pentavalent ion Mo^{5+}, which exhibits high affinity for oxygen.[15] Because semiconductor hydrogen sensors operate through the reaction between the hydrogen molecule and absorbed oxygen, Mo^{5+} may enhance the absorption of oxygen species on the surface of MoO_3 and, hence, the hydrogen sensing performance. Recently, Alsaif et al. has prepared the hydrogen sensor based on 2D α-MoO_3 nanoflakes that exhibited high sensitivity and fast responses to 1% of H_2 gas at 50 °C.[16] The large number of grain boundaries between the assembled nanoflakes may decrease the response speed at lower temperature possibly because of the slower hydrogen or oxygen diffusion at grain boundaries than at surface. Therefore, the RT hydrogen sensing performance of α-MoO_3 may be further improved by employing 1D MoO_3 nanostructures that reduce grain boundaries. There are many techniques to synthesize MoO_3 1D nanostructures such as sputtering process, flame synthesis, chemical vapor deposition, thermal evaporation, and hydrothermal attempting. Among them, the hydrothermal method has advantages of low cost, high production throughput, and high controllability in structure and morphology. For example, Shakir and workers synthesized MoO_3 nanowires with a large length−diameter ratio using a facile one-pot hydrothermal method.[17] Unfortunately, they did not characterize the RT hydrogen sensing performance of MoO_3 1D nanostructure, nor did they consider the influence of the synthesis process on its sensing properties.

In this paper, α-MoO_3 nanoribbons of various sizes were synthesized by hydrothermal method at different reaction temperatures. The nanoribbon sensors exhibit high RT sensing of hydrogen gas with a concentration of 0.5−1000 ppm. The RT hydrogen sensing performance of the nanoribbons is affected by the hydrothermal temperatures. The sensing mechanism has also been discussed in detail.

2. EXPERIMENTAL SECTION

2.1. Material Synthesis and Characterization. $Na_2MoO_4{\cdot}2H_2O$, HNO_3 and absolute ethanol were purchased from Sinopharm Chemical Reagent Co., Ltd. (Shanghai, China). All of the reagents were analytical grade and used as received without further purification. MoO_3 nanoribbons were synthesized by hydrothermal method. In a typical procedure, 0.01 mol $Na_2MoO_4{\cdot}2H_2O$ was dissolved in 32.75 mL of DI water, and the mixture was continuously stirred for 30 min at RT. After that, about 2.5 mol/L of HNO_3 was added in the above solution with further stirring for another 10 min. The final limpid reaction solution was then transferred inside a Teflon-lined 50 mL stainless steel autoclave where it was kept at 200 °C for approximately 12 h and cooled naturally to RT in air. The product of white precipitate was collected after filtration, repeated DI water and absolute ethanol washing, and final drying at 70 °C for 12 h. For comparison, a series of MoO_3 nanoribbons were prepared at different reaction temperature.

The phases of the products were examined by X-ray diffraction (XRD, Bruker D8A25, CuK, λ = 1.5406 Å). The morphology and microstructure were characterized by field-emission scanning electron microscopy (FESEM, JEOL JSM7100F) and high-resolution transmission electron microscopy (HRTEM, JEOL JEM 2010). X-ray photoelectron spectroscopy (XPS) experiments were conducted with a VG ESCALAB-MK electron spectrometer using Cu Kα radiation. Surface area and porosity were extracted by Brunauer−Emmett−Teller (BET) measurements using Quantachrome Nova 1200 with N_2 as the adsorbate at liquid nitrogen temperature.

2.2. Sensor Fabrication and Measurement. For the gas sensing test, a mixture of alcohol and as-obtained product was prepared. Then, the paste was applied to a pair of comb-like electrodes with spacing of 100 μm that were formed by sputtering 120 nm thick Pt−Ti alloy (80−20% by thickness) on the quartz substrate (1.0 cm × 1.0 cm). Then the assembly was heated at 200 °C for 2 h in vacuum to form the sensor. The RT gas sensing properties were measured by monitoring the change of the sensor resistance in a multimeter (Keithley 2400) with a working voltage of 1.0 V when the sensor was exposed to air or the test gas. In this study, we used a homemade measurement system to determine the sensing properties to 0.5−1000 ppm hydrogen and its selectivity in environments of 500 ppm of CO, C_2H_5OH, and CH_3COCH_3.

3. RESULTS AND DISCUSSIONS

3.1. Materials Characterizations. The XRD patterns of as-synthesized powder at different reaction temperature are shown in Figure 1a. The diffraction peaks of all samples can be indexed to the orthorhombic phase of MoO_3 (JCPDS Card No. 05-0508). The sharp diffraction peaks at (020), (040), and (060) indicate the high crystallinity and orientation of the

DOI: 10.1021/acsami.5b01858
ACS Appl. Mater. Interfaces 2015, 7, 9247−9253

samples. The intensity of (020) peak for nanoribbons synthesized at 200 °C is much stronger than that of other powder, a possible effect arising from reaction temperature on crystallinity and orientation. The refined lattice parameters show no noticeable difference for the samples prepared at various temperatures (c.f. Table 1), which indicates that the temperature does not affect the lattice parameters. The average thickness of nanoribbons along the [010] direction was estimated by Scherrer equation for peaks ranging from 39 to 40° (Table 1). The SEM images of the assembled nanoribbons are presented in Figure 1b where ribbon-like structures are visible in all samples. The dispersity of nanoribbons improves with the reaction temperature, especially in the sample prepared at 200 °C, where a large number of highly dispersive and uniform nanoribbons can be observed. The distribution density and average length of the nanoribbons increase with the hydrothermal temperature as well.

Table 1. Refined Lattice Parameters and Mean Grain Size along the [010] Direction of the Samples

T (°C)	a (Å)	b (Å)	c (Å)	$D_{(010)}$ (nm)
120	3.9617(5)	13.8019(6)	3.6811(8)	27.5450
160	3.9453(7)	13.7947(6)	3.7131(9)	36.2760
180	3.9449(4)	13.8052(2)	3.7018(7)	41.8640
200	3.9460(1)	13.7865(6)	3.6980(2)	43.2490

Figure 2 shows the TEM and HRTEM images of individual MoO_3 nanoribbon obtained at different temperatures. The surfaces of all nanoribbons are smooth and contamination-free. The cross section widths are approximately 200 nm for the nanoribbons obtained at 120, 160, and 180 °C, and 311 nm for the 200 °C sample. The selected area electron diffraction (SAED) patterns shown in the inset pictures confirm the single-crystalline nature of the orthorhombic nanoribbons, consistent with the XRD results. The distinct lattice stripes in the HRTEM images imply good crystallinity. In the selected area of four samples, the calculated interlayer distances of (001) and (100) planes are 0.18 and 0.20 nm, which agree well with the theoretical values for orthorhombic MoO_3 and confirm the preferential growth along [001] direction regardless of the reaction temperature. The later conclusion is also supported by the increase of $D_{(010)}$ from the XRD patterns, and further corroborated by the visible change of contrast for each nanoribbon caused by different thickness. On the other hand, the faster growth rate at higher hydrothermal temperature may create Mo^{5+} ions, leading to more structural defects during the Ostwald-ripening process.

To identify the valence state of Mo and the non-stoichiometry in MoO_3 nanoribbons, we analyzed the samples by XPS. Figure 3a presents a series of XPS analysis of Mo 3d peaks for MoO_3 nanoribbons annealed at 200 °C in vacuum, where two patterns of Mo 3d are observed in each image. No peak corresponding to Mo metal has been detected.[18] Both Mo $3d_{5/2}$ and $3d_{3/2}$ peaks were fitted to two components. The dominant peaks shown in solid lines at 232.8 ± 0.1 and 236.1 ± 0.1 eV represent the major component corresponding to Mo^{6+} ions in four samples. The recessive peaks shown in dashed lines shift to lower binding energies and are attributed to Mo^{5+} ions.[19−21] The corresponding XPS spectra in the O ls energy region are shown in Figure 3b where peaks associated with oxides and chemisorbed oxygen can be distinguished. The peaks shown by solid lines at 530.8 ± 0.1 eV are assigned to lattice oxygen atoms of MoO_3, while the peaks at a higher binding energy 532.0 ± 0.1 eV are identified as those from the chemisorbed oxygen atoms (O_{chem}) on the surface of MoO_3.[18,21,22]

Table 2 summarizes the XPS Mo 3d and O 1s core levels in MoO_3 nanoribbons synthesized at different temperatures. The amount of Mo^{5+} and O_{chem} increase with increasing hydrothermal temperature, suggesting a strong correlation between the surface absorption of oxygen species and Mo^{5+} content.[15] The maximum Mo^{5+} and O_{chem} content are ~21 and 16%, respectively, for nanoribbons obtained at 200 °C. Moreover, the average length and specific surface area are also dependent on the hydrothermal temperature. As shown in Figure 4, both the average length and the BET surface areas of the nanoribbons increase with increasing hydrothermal temperatures, which means that the nanoribbons with longer length will have larger specific surface area and more effective active sites to the target gas. The longest average length 13.18 μm and largest BET surface area 13.02 m^2/g are observed in MoO_3 nanoribbons synthesized at 200 °C.

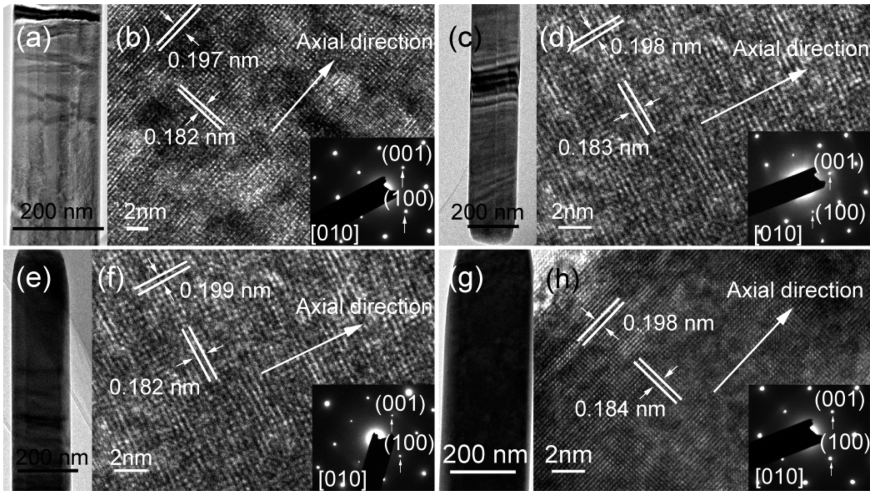

Figure 2. TEM and HRTEM images of as-synthesized MoO_3 nanoribbons obtained at (a and b) 120 °C, (c and d) 160 °C, (e and f) 180 °C, and (g and h) 200 °C; (insets) corresponding SAED patterns.

DOI: 10.1021/acsami.5b01858
ACS Appl. Mater. Interfaces 2015, 7, 9247−9253

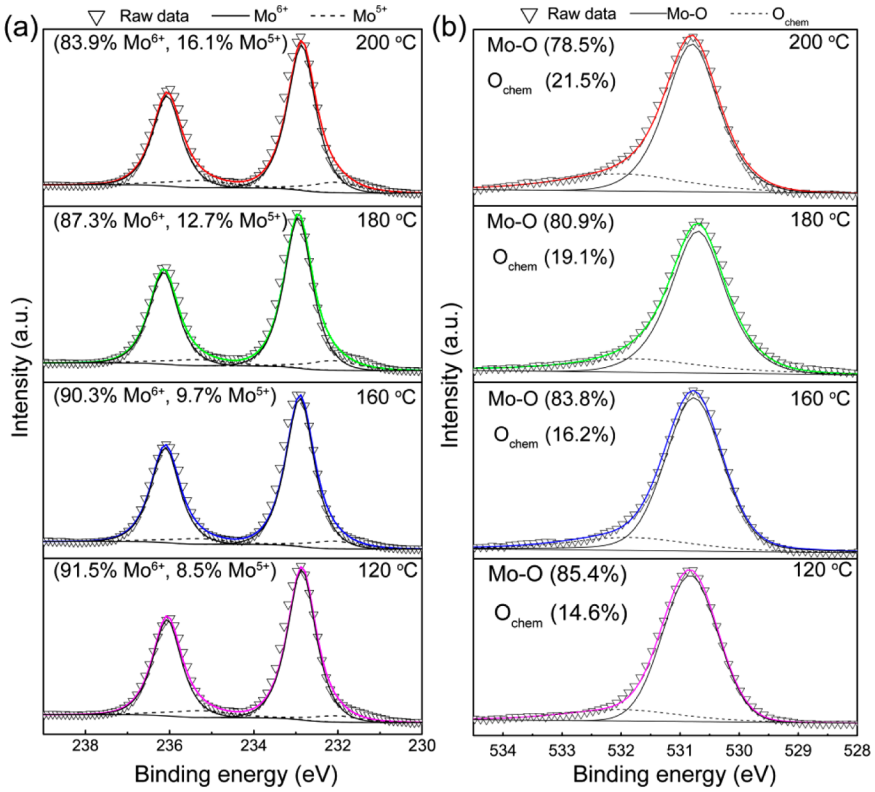

Figure 3. XPS of (a) Mo 3d and (b) O 1s core level spectra of MoO_3 nanoribbons synthesized at different temperature.

Table 2. XPS Mo 3d and O 1s Core Levels in MoO_3 Synthesized at Different Temperature

	Mo 3d core levels (%)		O 1s core levels (%)	
synthesized temp (°C)	Mo^{6+}	Mo^{5+}	Mo−O	O_{chem}
120	91.5	8.50	85.4	14.6
160	90.3	9.70	83.8	16.2
180	87.3	12.7	80.9	19.1
200	83.9	16.1	78.5	21.5

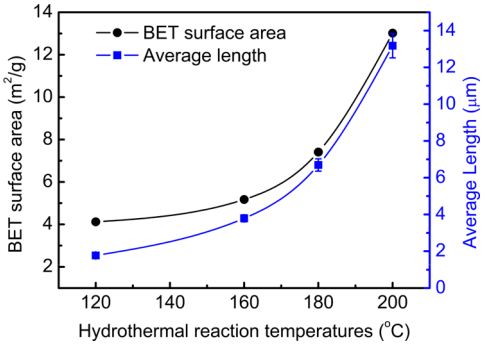

Figure 4. Average lengths and the BET surface areas of the nanoribbons placed on the different sensors.

3.2. RT H_2 Sensing Properties. To investigate the hydrogen sensing properties, we directly assembled the as-synthesized nanoribbons on the Pt/Ti interdigital electrodes and denoted as S4 to S1 for hydrothermal temperature at 120, 160, 180, and 200 °C, respectively. After the heat treatment, the sensors were placed in a homemade apparatus to evaluate their gas sensing properties. In this paper, the gas response sensitivity factor (S) is defined as $S = \Delta R/R_{air} = (R_{air} - R_{gas})/R_{air}$, where ΔR is the difference between the resistance in air (R_{air}) and in target gas (R_{gas}). The response time (t_{res}) and recovery time (t_{rec}) are defined as the time required for the sensor to reach 90% of the final response and recovery, respectively.

Figure 5a displays the RT hydrogen sensing properties of the sensors to 500 ppm of H_2 in air. The inset is a schematic illustration of the as-fabricated sensor made from MoO_3 nanoribbons. All assembled devices reacted quickly to the injection and evacuation of the target gas and the sensitivity factor S increased when the sensors were exposed to hydrogen containing atmosphere. As shown in Figure 5b, both the sensitivity and response/recovery speed are enhanced by the hydrothermal temperature. The maximum sensitivity ~0.85 is found in S1. The response time ranges from 21 to 69 s, and the recovery time ranges from 75 to 150 s for S1−S4.

The response performance of S1 to hydrogen concentrations from 1000 to 0.5 ppm is shown in Figure 6a and b. The response sensitivity increases with increasing hydrogen concentration and is stable due to the gradual saturation of adsorbed hydrogen. The maximum sensitivity is 90% for 1000 ppm of H_2 and is much larger than that for 5 ppm (S = 19%). Table 3 lists the response time of the reported semiconductor 1D nanomaterials. In comparison, the response time of our MoO_3 nanoribbon-based hydrogen sensors is shorter than that reported in previous work.[23−25] The response time to 1000 ppm hydrogen is only 14.1 s which is much faster than that of 2D nanoflakes based sesnor (30 s to 1% H_2 at 50 °C). According to the national standard of the People's Republic of China (GB 15322.1-2003), the standard response time can be defined as the time needed for the sensor to reach 90% of the final response when the gas concentration is 60% of its full detection range, which is 18.7 s at 600 ppm of H_2 for our MoO_3 sensor. Moreover, the standard response time for alarming of

DOI: 10.1021/acsami.5b01858
ACS Appl. Mater. Interfaces 2015, 7, 9247−9253

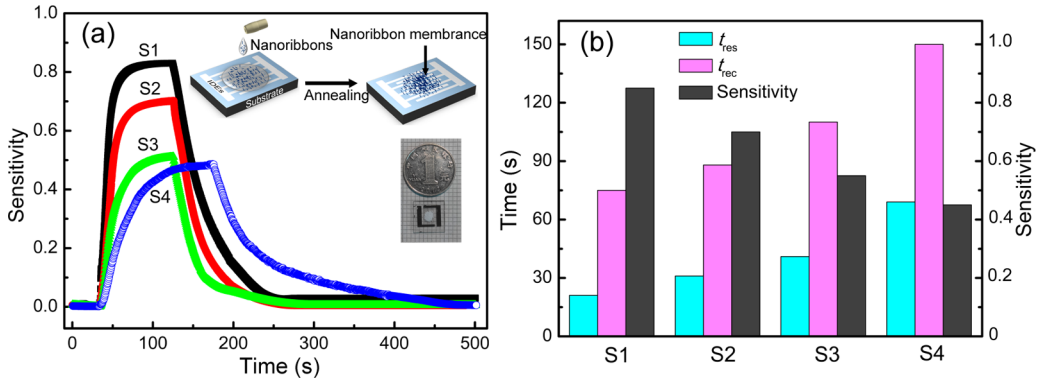

Figure 5. (a) Dynamic response of different MoO_3 sensors toward 500 ppm of H_2; (inset) schematic illustration of the fabrication process and the as-fabricated sensor. (b) Sensitivity, response time, and recovery time of different MoO_3 sensors.

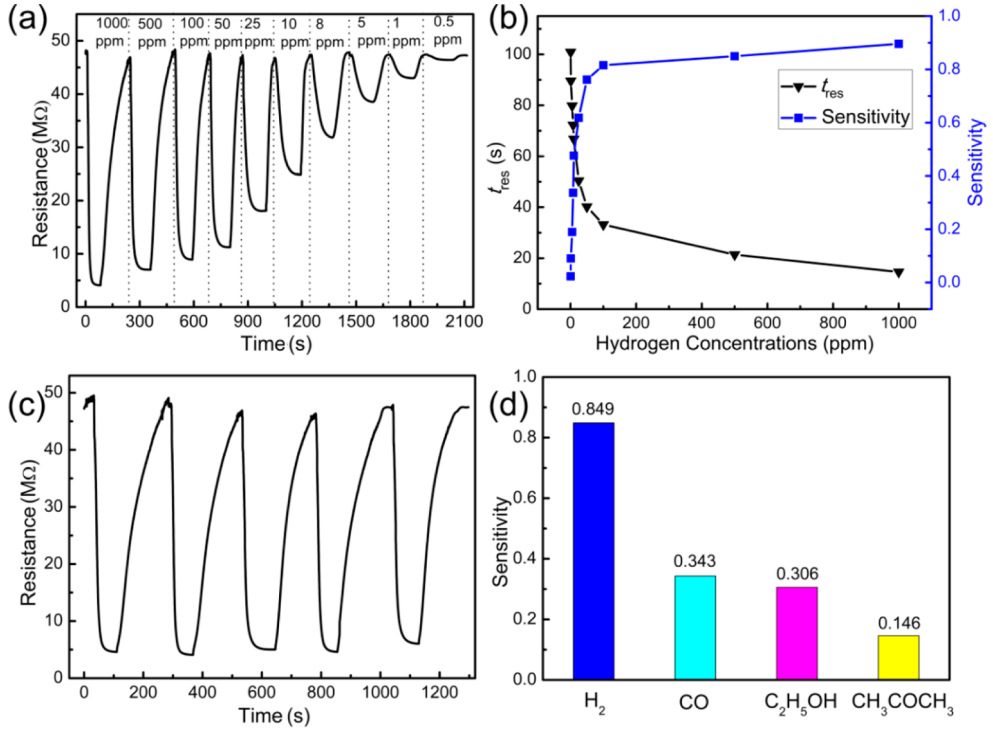

Figure 6. Hydrogen response and selectivity of S1 measured at RT. (a) Dynamic response resistances to different concentration of H_2; (b) H_2 concentration-dependent t_{res} and sensitivity of the Pt/MoO_3 nanoribbons sensor; (c) five response cycles to 1000 ppm of H_2; and (d) the gas response to different gases of 500 ppm.

Table 3. Response Time of Recent Developed Semiconductor 1D Nanostructures without Doping and Decoration

materials	$t_{response}$ (s)	temp (°C)	conc (ppm)	ref
MoO_3 nanoribbons	14.1	RT	1000	this work
ZnO nanorods	60	RT	1000	8
Nb_2O_5 nanowires	130	RT	1000	28
Pd decorated Nb_2O_5 nanowires	473	RT	1000	9
ZnO nanorods textile	600	RT	1000	29

MoO_3 is ~16.4 s, that is the response time for H_2 concentration of 1.6 times higher than the set alarm value (500 ppm) which is required to be not lower than 1% of low explosive limit (LEL, 4% for hydrogen). Therefore, the MoO_3 nanoribbon-based sensor can meet the basic requirements for both the alarm apparatus and the concentration monitors that have the standard response time threshold of 30 s. Moreover, the sensor also exhibits outstanding repeatability according to Figure 6c. To test the selectivity to H_2, we investigated our sensor's sensitivity to a variety of potential interferential gases of CO, C_2H_5OH, and CH_3COCH_3. As shown in Figure 6d, the sensitivity toward CO, C_2H_5OH, and CH_3COCH_3 is much lower than that to hydrogen, underscoring a remarkably high selectivity toward H_2. The sensing performance of our sensor to all the target gases could be attributed to the redox reaction with the surface absorbed oxygen species.[26] First, the diameters of ethanol and acetone molecules are much larger than those of H_2 and CO. It is difficult for the larger molecules to penetrate into the inner layer of the nanoribbon membrane and react with the chemisorbed oxygen. Second, the bond energy of H_2 is 436 kJ/mol, much lower than that of CO (1072 kJ/mol). Therefore, it is easier to open the bond in H_2 at lower

DOI: 10.1021/acsami.5b01858
ACS Appl. Mater. Interfaces 2015, 7, 9247−9253

temperature. As a result, the MoO_3 nanoribbons exhibit higher response to hydrogen against CO, ethanol and acetone.[27]

3.3. Sensing Mechanism. In previous reports, the depletion-layer-modulation model has been used to explain the sensing mechanism of metal-oxide nanowires.[30,31] Here, we adopt the same model to study the relation between the gas response and MoO_3 nanoribbons. The intrinsic sensing property of MoO_3 nanoribbons arises from Mo^{5+} ion induced structural defects,[15,32] where Mo^{5+} ions act as adsorbing centers with high affinity to gases. When the sensor is placed in the atmosphere, the oxygen molecules will spontaneously adsorb onto the nanoribbon surface as

$$O_2(g) \leftrightarrow O_2(ad) \quad (1)$$

As shown in Figure 7, the chemisorption of oxygen species will trap the free electrons near the surface area via

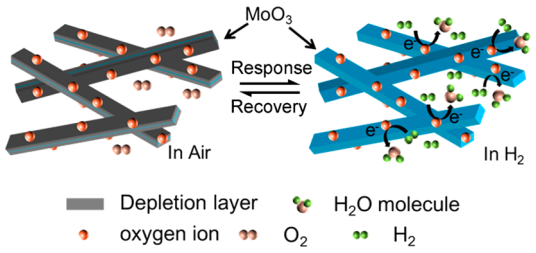

Figure 7. Schematic diagram of the H_2 sensing mechanism of MoO_3 nanoribbons.

$$O_2(ad) + e^- \rightarrow O_2^-(ad) \quad (2)$$

and cause electron depletion at surface, leading to reduced free charge carrier density and increased resistance. Thereafter, H_2 is injected into the system and reacts with the chemisorbed oxygen ions through

$$2H_2 + O_2^-(ad) \rightarrow 2H_2O + e^- \quad (3)$$

which releases the previously trapped electrons to the conduction band of MoO_3 surface, reduces thickness of the depletion region, and enhances electrical conductivity. When the sensors are exposed in air again, the oxygen molecules will be re-adsorbed on the nanoribbons (primarily at the position of Mo^{5+}) and prompt the reconstruction of the depletion region.[15] This model can satisfactorily explain the complete recovery behavior of the hydrogen response.

Figure 8 shows the relation among the Mo^{5+} content, O_{chem} content and the sensitivity of the α-MoO_3 hydrogen sensors. As reported, the Mo^{5+} in α-MoO_3 lattice is the favorite absorption site for oxygen species.[25,30,33] The increased content of Mo^{5+} from higher hydrothermal temperature will lead to more chemisorbed oxygen on the surface of the nanoribbons (red curve). Indeed, the sensitivity exhibits linear correlation with respect to the O_{chem} content (blue curve), in agreement with the enhanced reaction due to larger amount of chemisorbed oxygen (eq 3).[8,14] In addition, the higher specific surface area provides more absorption sites for the oxygen species, another factor contributing to the improved hydrogen sensing performance for nanoribbons prepared at high hydrothermal temperature. Moreover, during the recovery process, the surface absorbed oxygen ions will slowly diffuse into the interfaces between the adjacent nanoribbons due to the concentration difference. This diffusion process is much slower than the reaction between the hydrogen and oxygen ions. Therefore, the

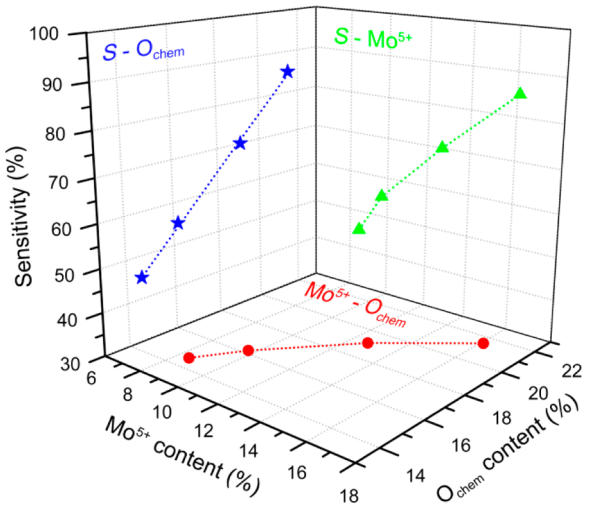

Figure 8. Relation among the sensitivity (S), Mo^{5+} content and O_{chem} content of the MoO_3 nanoribbons.

recovery time is much longer than the response time for all samples. Among them, shorter nanoribbons possess denser interfaces, lower special surface area and Mo^{5+} content. Hence, both the response and recovery process of products synthesized at 120 °C is much slower than other sensors.

4. CONCLUSIONS

α-MoO_3 nanoribbons were synthesized by hydrothermal method at temperatures ranging from 120 to 200 °C. All nanoribbons grew uniformly along the [001] direction. The increase of hydrothermal temperature leads to higher content of Mo^{5+} and chemisorbed oxygen, as well as enhanced H_2 sensing performance. Among them, the MoO_3 nanoribbons obtained at 200 °C exhibits highly responsive RT hydrogen sensing performance. The fastest response time is 14.1 s toward 1000 ppm of H_2. The sensors also boast good selectivity against CO, ethanol, and acetone. The lowest detectable H_2 concentration is 500 ppb. The hydrogen sensing behavior is dependent on the redox reaction between the H_2 and chemisorbed oxygen species. Higher hydrothermal temperature creates more Mo^{5+} ions, leading to increased specific surface area and chemisorbed oxygen species at the nanoribbon surface.

AUTHOR INFORMATION

Corresponding Authors

*E-mail: yongming.hu09@gmail.com.
*E-mail: guhsh@hubu.edu.cn.

Author Contributions

The manuscript was written through contributions of all authors. All authors have given approval to the final version of the manuscript.

Notes

The authors declare no competing financial interest.

ACKNOWLEDGMENTS

This work was financially supported by the National Science Foundation of China (Grant Nos. 11474088, 61274073), the National High Technology Research and Development Program of China (Grant No. 2013AA031903) and the Key Project of Natural Science Foundation of Hubei Province of China (Grant No. 2013CFA043, 2014CFB557).

DOI: 10.1021/acsami.5b01858
ACS Appl. Mater. Interfaces 2015, 7, 9247−9253

REFERENCES

(1) Kahn, M. E. Fueling the Future. *Science* **2015**, *347*, 239−239.

(2) Russo, P. A.; Donato, N.; Leonardi, S. G.; Baek, S.; Conte, D. E.; Neri, G.; Pinna, N. Room-Temperature Hydrogen Sensing with Heteronanostructures Based on Reduced Graphene Oxide and Tin Oxide. *Angew. Chem. Int. Ed.* **2012**, *51*, 11053−11057.

(3) Lu, G.; Ocola, L. E.; Chen, J. Room-Temperature Gas Sensing Based on Electron Transfer between Discrete Tin Oxide Nanocrystals and Multiwalled Carbon Nanotubes. *Adv. Mater.* **2009**, *21*, 2487−2491.

(4) Mao, S.; Cui, S.; Yu, K.; Wen, Z.; Lu, G.; Chen, J. Ultrafast Hydrogen Sensing through Hybrids of Semiconducting Single-Walled Carbon Nanotubes and Tin Oxide Nanocrystals. *Nanoscale* **2012**, *4*, 1275−1279.

(5) Ryu, B.; Lee, Y. T.; Lee, K. H.; Ha, R.; Park, J. H.; Choi, H.-J.; Im, S. Photostable Dynamic Rectification of One-Dimensional Schottky Diode Circuits with a ZnO Nanowire Doped by H during Passivation. *Nano Lett.* **2011**, *11*, 4246−4250.

(6) He, J.; Hu, Y.; Wang, Z.; Lu, W.; Yang, S.; Wu, G.; Wang, Y.; Wang, S.; Gu, H.; Wang, J. Hydrothermal Growth and Optical Properties of Nb_2O_5 Nanorod Arrays. *J. Mater. Chem. C* **2014**, *2*, 8185−8190.

(7) Yin, Y. X.; Jiang, L. Y.; Wan, L. J.; Li, C. J.; Guo, Y. G. Polyethylene Glycol-Directed SnO_2 Nanowires for Enhanced Gas-Sensing Properties. *Nanoscale* **2011**, *3*, 1802−1806.

(8) Hassan, J. J.; Mahdi, M. A.; Chin, C. W.; Abu-Hassan, H.; Hassan, Z. Room Temperature Hydrogen Gas Sensor Based on ZnO Nanorod Arrays Grown on a SiO_2/Si Substrate via a Microwave-Assisted Chemical Solution Method. *J. Alloys Compd.* **2013**, *546*, 107−111.

(9) Park, S.; Kim, S.; Hyun, S. K.; Lee, C. Room Temperature Hydrogen Sensing Properties of Multiple-Networked Nb_2O_5-Nanorod Sensors Decorated with Pd Nanoparticles. *J. Korean Phys. Soc.* **2014**, *65*, 1414−1418.

(10) Wang, B.; Zhu, L. F.; Yang, Y. H.; Xu, N. S.; Yang, G. W. Fabrication of a SnO_2 Nanowire Gas Sensor and Sensor Performance for Hydrogen. *J. Phys. Chem. C* **2008**, *112*, 6643−6647.

(11) Lee, J. M.; Park, J. E.; Kim, S.; Kim, S.; Lee, E.; Kim, S. J.; Lee, W. Ultra-Sensitive Hydrogen Gas Sensors Based on Pd-Decorated Tin Dioxide Nanostructures: Room Temperature Operating Sensors. *Int. J. Hydrogen Energy* **2010**, *35*, 12568−12573.

(12) Phuruangrat, A.; Ham, D. J.; Thongtem, S.; Lee, J. S. Electrochemical Hydrogen Evolution over MoO_3 Nanowires Produced by Microwave-Assisted Hydrothermal Reaction. *Electrochem. Commun.* **2009**, *11*, 1740−1743.

(13) Mai, L. Q.; Hu, B.; Chen, W.; Qi, Y. Y.; Lao, C. S.; Yang, R. S.; Dai, Y.; Wang, Z. L. Lithiated MoO_3 Nanobelts with Greatly Improved Performance for Lithium Batteries. *Adv. Mater.* **2007**, *19*, 3712−3716.

(14) Chithambararaj, A.; Sanjini, N. S.; Velmathi, S.; Bose, A. C. Preparation of *h*-MoO_3 and Alpha-MoO_3 Nanocrystals: Comparative Study on Photocatalytic Degradation of Methylene Blue under Visible Light Irradiation. *Phys. Chem. Chem. Phys.* **2013**, *15*, 14761−14769.

(15) Ivanovskaya, M.; Gurlo, A.; Bogdanov, P. Mechanism of O_3 and NO_2 Detection and Selectivity of In_2O_3 Sensors. *Sens. Actuators, B* **2001**, *77*, 264−267.

(16) Alsaif, M. M. Y. A.; Balendhran, S.; Field, M. R.; Latham, K.; Wlodarski, W.; Ou, J. Z.; Kalantar-zadeh, K. Two Dimensional α-MoO_3 Nanoflakes Obtained Using Solvent-Assisted Grinding and Sonication Method: Application for H_2 Gas Sensing. *Sens. Actuators, B* **2014**, *192*, 196−204.

(17) Shakir, I.; Shahid, M.; Yang, H. W.; Kang, D. J. Structural and Electrochemical Characterization of α-MoO_3 Nanorod-Based Electrochemical Energy Storage Devices. *Electrochim. Acta* **2010**, *56*, 376−380.

(18) Choi, J.-G; Thompson, L. T. XPS Study of As-Prepared and Reduced Molybdenum Oxides. *Appl. Surf. Sci.* **1996**, *93*, 143−149.

(19) Bai, S.; Chen, S.; Chen, L.; Zhang, K.; Luo, R.; Li, D.; Liu, C. C. Ultrasonic Synthesis of MoO_3 Nanorods and Their Gas Sensing Properties. *Sens. Actuators, B* **2012**, *174*, 51−58.

(20) Vasilopoulou, M.; Douvas, A. M.; Georgiadou, D. G.; Palilis, L. C.; Kennou, S.; Sygellou, L.; Soultati, A.; Kostis, I.; Papadimitropoulos, G.; Davazoglou, D.; Argitis, P. The Influence of Hydrogenation and Oxygen Vacancies on Molybdenum Oxides Work Function and Gap States for Application in Organic Optoelectronics. *J. Am. Chem. Soc.* **2012**, *134*, 16178−16187.

(21) Chen, H. Y.; Su, H. C.; Chen, C. H.; Liu, K. L.; Tsai, C. M.; Yen, S. J.; Yew, T. R. Indium-Doped Molybdenum Oxide As a New P-Type Transparent Conductive Oxide. *J. Mater. Chem.* **2011**, *21*, 5745−5752.

(22) Szuber, J.; Czempik, G.; Larciprete, R.; Koziej, D.; Adamowicz, B. XPS Study of the L-CVD Deposited SnO_2 Thin Films Exposed to Oxygen and Hydrogen. *Thin Solid Films* **2001**, *391*, 198−203.

(23) Ren, S.; Fan, G.; Qu, S.; Wang, Q. Enhanced H_2 Sensitivity at Room Temperature of ZnO Nanowires Functionalized by Pd Nanoparticles. *J. Appl. Phys.* **2011**, *110*, 084312.

(24) Kukkola, J.; Mohl, M.; Leino, A.-R.; Mäklin, J.; Halonen, N.; Shchukarev, A.; Konya, Z.; Jantunen, H.; Kordas, K. Room Temperature Hydrogen Sensors Based on Metal Decorated WO_3 Nanowires. *Sens. Actuators, B* **2013**, *186*, 90−95.

(25) Francioso, L.; Taurino, A. M.; Forleo, A.; Siciliano, P. TiO_2 Nanowires Array Fabrication and Gas Sensing Properties. *Sens. Actuators, B* **2008**, *130*, 70−76.

(26) Guo, X.; Kang, Y.; Wang, L.; Liu, X.; Zhang, J.; Yang, T.; Wu, S.; Wang, S. Mesoporous Tin Dioxide Nanopowders Based Sensors to Selectively Detect Ethanol Vapor. *Mater. Sci. Eng., C* **2011**, *31*, 1369−1373.

(27) Caihong, W.; Xiangfeng, C.; Mingmei, W. Detection of H_2S Down to ppb Levels at Room Temperature Using Sensors Based on ZnO Nanorods. *Sens. Actuators, B* **2006**, *113*, 320−323.

(28) Wang, Z.; Hu, Y.; Wang, W.; Zhang, X.; Wang, B.; Tian, H.; Wang, Y.; Guan, J.; Gu, H. Fast and Highly-Sensitive Hydrogen Sensing of Nb_2O_5 Nanowires at Room Temperature. *Int. J. Hydrogen Energy* **2012**, *37*, 4526−4532.

(29) Lim, Z. H.; Chia, Z. X.; Kevin, M.; Wong, A. S. W.; Ho, G. W. A Facile Approach towards ZnO Nanorods Conductive Textile for Room Temperature Multifunctional Sensors. *Sens. Actuators, B* **2010**, *151*, 121−126.

(30) An, X.; Yu, J. C.; Wang, Y.; Hu, Y.; Yu, X.; Zhang, G. WO_3 Nanorods/Graphene Nanocomposites for High-Efficiency Visible-Light-Driven Photocatalysis and NO_2 Gas Sensing. *J. Mater. Chem.* **2012**, *22*, 8525.

(31) Gu, H.; Wang, Z.; Hu, Y. Hydrogen Gas Sensors Based on Semiconductor Oxide Nanostructures. *Sensors* **2012**, *12*, 5517−5550.

(32) Sunu, S. S.; Prabhu, E.; Jayaraman, V.; Gnanasekar, K. I.; Seshagiri, T. K.; Gnanasekaran, T. Electrical Conductivity and Gas Sensing Properties of MoO_3. *Sens. Actuators, B* **2004**, *101*, 161−174.

(33) Kadir, R. A.; Rani, R. A.; Zoolfakar, A. S.; Ou, J. Z.; Shafiei, M.; Wlodarski, W.; Kalantar-zadeh, K. Nb_2O_5 Schottky Based Ethanol Vapour Sensors: Effect of Metallic Catalysts. *Sens. Actuators, B* **2014**, *202*, 74−82.

DOI: 10.1021/acsami.5b01858
ACS Appl. Mater. Interfaces 2015, 7, 9247−9253